Continental Shelf Research 170 (2018) 21–32

Contents lists available at ScienceDirect

Continental Shelf Research

journal homepage: www.elsevier.com/locate/csr

Research papers

Field observations of turbulence in the intertidal and shallow subtidal zones

Drude F. Christensen[a,*], Joost Brinkkemper[b,c], Gerben Ruessink[b], Troels Aagaard[a]

[a] Department of Geosciences and Natural Resource Management, University of Copenhagen, Øster Voldgade 10, DK-1350 Copenhagen, Denmark
[b] Department of Physical Geography, Utrecht University, P.O. Box 80.115, 3508 TC Utrecht, Netherlands
[c] WaterProof Marine Consultancy and Services BV, Ijsselmeerdijk 2, 8221 RC Lelystad, Netherlands

ARTICLE INFO

Keywords:
Near-shore processes
Turbulence
Spilling breakers
Surf bores
Bed forms
Field experiment

ABSTRACT

Turbulence is critical for sediment mobilisation in shallow water and hence beach evolution. Present large-scale morphological models often exclude the effects of bed- and surface-generated turbulence on the short-wave sediment transport, which might be part of the reason why they tend to result in incorrect estimates of the onshore-directed sediment transport under low-energetic conditions. A first step for model improvements is to be able to couple turbulence intensity and orbital motion at intra-wave time scale. Field measurements of flow velocities at three vertical elevations at two cross-shore locations in the intertidal and shallow subtidal zones were used to examine turbulence beneath shoaling waves, spilling breakers and surf bores. Beneath shoaling waves, near-bed turbulent kinetic energy (*TKE(t)*) was generated by bed friction and phase-coupled to the cross-shore orbital velocity ($u(t)$). Beneath spilling breakers, turbulence intensity increased, especially in the upper part of the water column due to injection of breaker-generated turbulence. The surface-induced *TKE(t)* peaked just after the wave crest. Near the bed, *TKE(t)* had a broad maximum under the wave trough possibly due to increased shear from stronger offshore-directed mean currents. Beneath surf bores, *TKE(t)* peaked at the wave front throughout the water column which could be due to both acceleration skewness and a turbulent bore front.

1. Introduction

It is well known that sandy beaches undergo continuous cyclic changes of erosion and accretion due to redistribution of sand by waves and currents (Shepard, 1950). Turbulent motions induced by wave breaking or friction at the seabed are critical for sediment mobilisation and subsequent transport. Turbulent eddies both enhance shear stresses that bring sediment in suspension, and enhance the vertical mixing of sediment (e.g. Nielsen, 1992; Beach and Sternberg, 1996; Aagaard and Hughes, 2013). Generation of turbulence, at both the bed and sea surface, is a very intermittent process which complicates the phase relationship between wave orbital motion and suspended sediment concentration (e.g. van der Werf et al., 2007; Yoon and Cox, 2012; Brinkkemper et al., 2017a). Presently available morphodynamic models have not often incorporated these effects (e.g. van Rijn et al., 2013) which might underlie the limited predictive ability of the models in onshore bar migration during low-energetic conditions (e.g. Henderson et al., 2004; Mariño-Tapia et al., 2007; Ruessink and Kuriyama, 2008). Being able to couple turbulence intensity and orbital motion at an intra-wave time scale provides a basis for model improvements.

Studies on turbulence production have mostly been conducted in laboratory flumes while field experiments are scarcer. For surface-induced turbulence, the wave breaker type has proved decisive for turbulence intensity, vertical mixing and temporal variation within the wave cycle (e.g. Ting and Kirby, 1994; Aagaard and Hughes, 2010; Brinkkemper et al., 2016). Turbulence intensity and vertical mixing is largest beneath plunging breakers where large, coherent plunger vortices are generated, and successions of turbulent eddies are instantly transported towards the bottom, increasing the local instantaneous bed shear stress (e.g. Ting and Kirby, 1995). The strong vertical mixing implies that vertical profiles of turbulent kinetic energy (*TKE*) are almost depth uniform (Ting and Kirby, 1994; Yoon and Cox, 2010; Grasso et al., 2012; Brinkkemper et al., 2016).

In spilling breakers, two-dimensional turbulent eddies are produced in a surface roller which break down through the formation of three-dimensional obliquely descending eddies that appear behind the wave crest (Nadaoka et al., 1989). The vertical mixing rate under spilling breakers is smaller than beneath plunging breakers, and vertical profiles of *TKE* exhibit a decrease towards the bed (Ting and Kirby, 1994; Yoon and Cox, 2010). The slow mixing along with large turbulence decay times imply that the turbulence is not dissipated over one wave period (Ting and Kirby, 1994). This results in less temporal variations in *TKE* over the wave cycle compared to plunging breakers where decay times are shorter (Ting and Kirby, 1994). The slow penetration of *TKE*

* Corresponding author.
E-mail address: dc@ign.ku.dk (D.F. Christensen).

https://doi.org/10.1016/j.csr.2018.10.002
Received 21 March 2018; Received in revised form 14 August 2018; Accepted 4 October 2018
Available online 12 October 2018

through the water column furthermore results in a later near-bed maximum *TKE* within the wave cycle compared to plunging breakers, i.e. a larger phase-lag between cross-shore orbital velocity (u) and *TKE* (Ting and Kirby, 1994, 1996; Scott et al., 2009; Aagaard and Hughes, 2010). Scott et al. (2009) even observed largest near-bed *TKE* beneath the wave trough for spilling breakers, which consequently lead to an offshore-directed transport of turbulence by the short-wave orbital motion. In the inner surf zone, studies of field and field-scale laboratory surf bore conditions are relatively scarce, but, for instance, Butt et al. (2004) observed turbulence mainly produced on the wave front. The vertical mixing is expected to be faster under surf bores compared to spilling breakers, thereby leading to a more homogeneous water column and smaller phase-lag (Peregrine and Svendsen, 1978; Sou and Yeh, 2011).

Beneath shoaling waves, bed friction is the primary source of turbulence. The intensity of the bed-generated turbulence is a function of both flow velocity and bed roughness. The latter depends on the sediment grain size and presence/geometry of bed forms. According to Nielsen (1992), for a larger ripple steepness, the bed roughness and hence the turbulence intensity also increase. Nichols and Foster (2007) on the other hand, relate near-bed vortex strength (i.e. turbulence intensity) to ripple height through the Keulegan-Carpenter number. Ripple height and steepness both relate inversely with wave orbital velocity as stronger flow velocity produces flatter ripples. This means that the near-bed turbulence level is of similar magnitude for different bed states (Smyth and Hay, 2003). The bed form dimensions are, however, of importance for the temporal variation of the turbulence intensity within the wave cycle. In the presence of vortex ripples, a vortex is generated between the ripple crests, and it remains trapped at the bed by the free stream flow until flow reversal (van der Werf et al., 2007). At this moment, the vortex is ejected from the bed resulting in increased *TKE* at the times of flow reversal. For velocity-skewed waves, the larger velocities beneath the wave crest result in ejection of more energetic turbulent eddies at the on- to offshore velocity reversal compared to off- to onshore velocity reversal. As the turbulent eddies entrain suspended sediment, the suspended sediment concentration becomes largest beneath the wave trough. The turbulent eddies thereby affect both the magnitude and direction of short-wave sediment transport (e.g. O'Hara Murray et al., 2011).

In this paper, field observations of turbulence measured at different vertical elevations at two cross-shore locations in the intertidal and shallow subtidal zones are reported. The main aims of the paper are to identify the dominant sources of turbulence and investigate the intra-wave variations of *TKE* as it is of importance for the timing of sediment suspension and eventually transport. Variability of turbulence characteristics in the cross-shore will be examined based on measurements from the two instrument rigs located twelve meters apart in the surf zone. Most of the earlier papers discussing measurements of turbulence in a natural surf zone (e.g. Butt et al., 2004; Aagaard and Hughes, 2010; Ruessink, 2010) do this based on one cross-shore location and can therefore only relate turbulence characteristics to H_s/h, which does not necessarily present variability in the cross-shore. Moreover, the majority of the previous mentioned research on surf zone turbulence is based on experiments conducted in laboratory flumes (e.g. Scott et al., 2005; Brinkkemper et al., 2017a; van der A et al., 2017), so it is also a motivation of this study to investigate to which extent those findings from the laboratory are representing natural processes in the field.

2. Methods

2.1. Field site

The TASTI (Turbulence And Sand Transport Initiative) field experiment was conducted at the beach of Vejers on the Danish North Sea coast (Fig. 1). The shore-normal is oriented 285 °N, and the beach is exposed to wind and swell waves with a mean annual significant wave height, $H_s = 1.3$ m ($H_s = 4\sigma_\eta$ where σ_η is the standard deviation of the water surface elevation) at 16 m water depth (Aagaard and Hughes, 2010). The beach is modally intermediate (cf. Wright and Short, 1984) with several longshore bars on the upper shoreface (Aagaard and Hughes, 2010). The tide is semidiurnal with spring and neap tidal ranges of approximately 1.2 m and 0.6 m (Aagaard and Hughes, 2010).

Data was collected from September 17 to October 10, 2016, at two positions, twelve meters apart, between the intertidal bar and the inner subtidal bar (i.e. in the zone ranging from -0.75 m to -0.25 m relative to mean sea level) (Fig. 2). The subtidal rig (the most seaward rig) was, however, retrieved on September 25 due to significant instrument burial. Data obtained after September 25 is therefore not used in this paper. The sediment at the position of the subtidal rig was fine, well sorted sand with a mean sediment grain size of 188 μm, while the mean grain size at the intertidal rig (the most landward rig) was 211 μm. During September 17 to September 25, the offshore significant wave height ranged between 0.28 m and 1.5 m, and the mean wave period was between 2.7 s and 9.5 s (Fig. 3).

The predominant wave conditions at the two instrument positions were observed to be markedly different during the campaign. The subtidal rig was mostly located in the shoaling or outer surf zones, and non-breaking waves and spilling breakers were the dominant wave types. The intertidal rig was typically located in the inner surf zone dominated by surf bores at high tide and on the dry beach at low tide. Since this station was periodically exposed at every low tide, bed forms were reset at the beginning of each tidal cycle due to swash motions, while at the subtidal rig bed forms persisted through wave cycles. Owing partly to these circumstances, the data sets from the two rigs are treated individually throughout the paper.

2.2. Instrumentation

The two rigs were both equipped with a pressure transducer (TD) to obtain mean water level and wave height, three vertically separated Acoustic Doppler Velocimeters (ADVs) to measure flow velocities throughout the water column, (fiber) optical backscatter sensors ((F)OBS) to estimate the suspended sediment concentration and sonars to monitor bed forms.

The subtidal rig consisted of an elevated square platform carrying data loggers and batteries with a lower, triangular extension pointing seaward where the instruments were mounted. Two Sontek 5 MHz ADVOcean were oriented sideways and initially placed about 0.50 m (ADV3) and 0.20 m (ADV2) above the bed, while a 3-D sideways looking Sontek 10 MHz ADV was placed 0.10 m above the bed (ADV1). All ADVs were recording at 10 Hz and were oriented to measure positive flows to the north, onshore and upwards. All the instruments recorded data for 30 min every hour. Bed morphology was monitored using both an Imagenex 881A Profiling Sonar which made continuous cross-shore scans, and an Imagenex 881A Imaging Sonar making rotational scans of the seabed every 20 min.

The intertidal rig consisted of a scaffold frame where loggers, batteries and instruments were mounted. Three downward-looking Sontek ADVOcean sensors, also recording at 10 Hz, were initially placed at 0.57 m (ADV3), 0.38 m (ADV2) and 0.28 m (ADV1) above the bed, with the measurement volumes located at 0.39 m, 0.20 m and 0.10 m above the bed. These ADVs were also oriented to measure positive flows to the north, onshore and upwards. Every half hour a float near the bed checked for submergence, and data logging started at the hour or at half past. For further information on the field campaign see Brinkkemper et al. (2017b).

2.3. Velocity data processing

2.3.1. Quality check and despiking

In the surf zone it is very common for ADV signals to become noisy due to the presence of air bubbles. The velocity signals have therefore

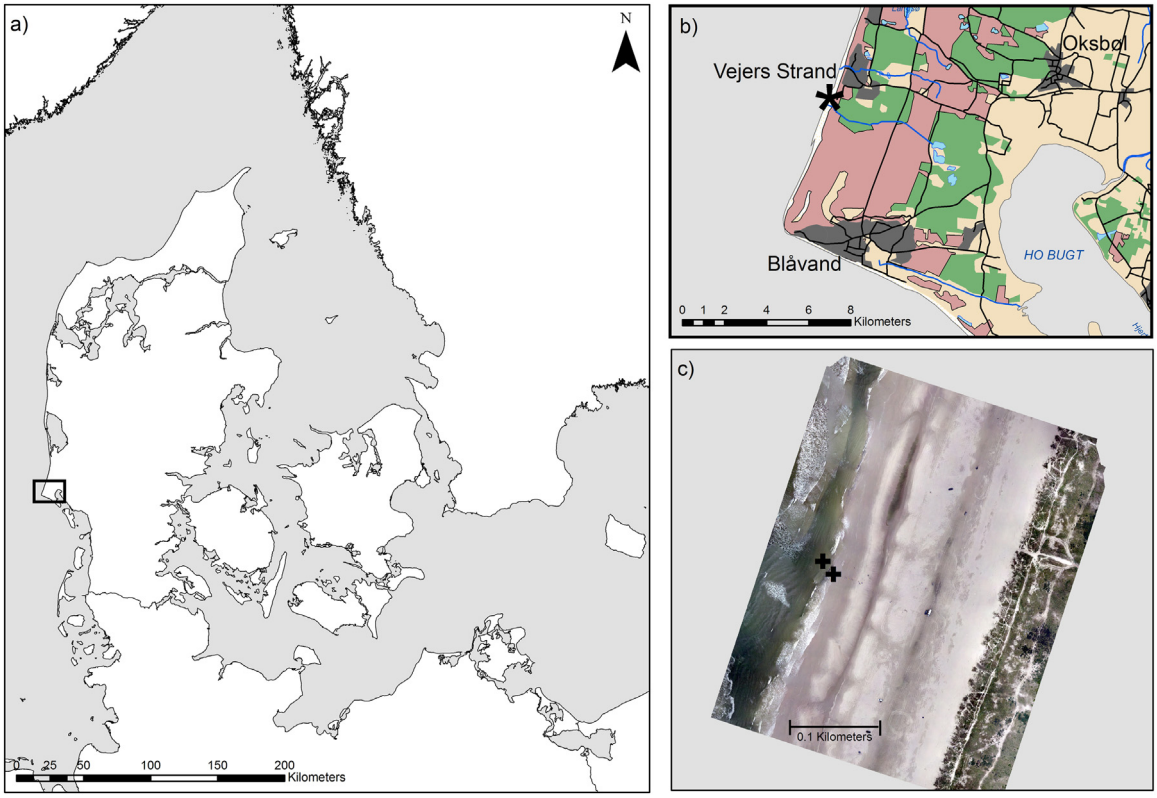

Fig. 1. a) Map of Denmark with the field site, Vejers, highlighted, b) enlarged map of Vejers and c) an aerial photo of the beach taken by a drone during low tide in the first week of the field campaign. The positions of the instrument rigs are marked by the crosses.

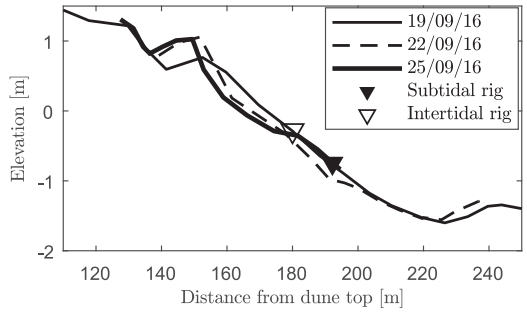

Fig. 2. Cross-shore profiles measured on September 19, 22 and 25, 2016. The positions of the instrument rigs are marked by the triangles. The intertidal rig is located at $x = 180$ m and the subtidal rig at $x = 192$ m.

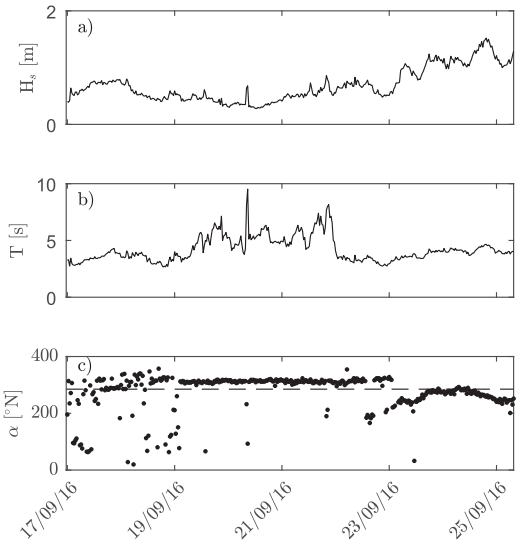

Fig. 3. a) Offshore significant wave height (H_s), b) mean wave period (T) and c) direction of wave propagation (α) for September 17 to September 25. The horizontal dashed line in the lower panel, c), marks the orientation of the shore-normal.

been quality checked and despiked. The data sets from the two rigs were treated in slightly different ways as air bubbles were a smaller problem at the subtidal rig. However, both data sets were quality checked based on the guidelines suggested by Elgar et al. (2005). At the intertidal rig, time series containing more than 5% backscattered signal amplitudes < 100 were rejected, while at the subtidal rig, only single-point signal amplitudes were validated, and signals with an amplitude < 147 (corresponding to a signal-to-noise ratio of 20) were rejected. Moreover, both data sets were controlled with reference to the correlation coefficients of the signals, and signals with correlations < 55 were rejected and interpolated with filtered values (using a 1 s low-pass box-filter).

At the intertidal rig, the time series were despiked with the phase-space method by Mori et al. (2007). Detected spikes were rejected and interpolated. At the subtidal rig, the signals were less noisy and the method by Mori et al. (2007) was considered to be too conservative. Therefore, a spike-threshold method was applied: spikes in the horizontal velocity components (u, v) were identified as cases when the change in velocity between adjacent data points ($u_i - u_{i-1}$) exceeded three times the standard deviation of the time series. For the vertical velocity components (w) the applied threshold for spike identification was half the acceleration of gravity, i.e. $(w_i - w_{i-1}) > \frac{1}{2}g$. Calculating the mean *TKE* of an example time series despiked by both two methods revealed a difference of about 7%.

In addition, both data sets were rotated in order to minimize small tilt errors of the velocity sensors. At the intertidal rig, the rotation was in accordance with measurements from the internal tilt sensor of the

ADVs (cf. Ruessink, 2010), while at the subtidal rig the procedure outlined in Emery and Thomson (2001) was applied:

$$\alpha_x = \sqrt{tan\left(\frac{2(u_{ds}w_{ds})}{(u_{ds}^2 - w_{ds}^2)}\right)} \quad (1)$$

$$w = w_{ds}\cos(\alpha_x) - u_{ds}\sin(\alpha_x) \quad (2)$$

where the subscript *ds* indicates that the velocities are despiked, α_x is the cross-shore vertical tilt and w is the corrected velocity vector. To correct for longshore vertical tilt, u_{ds} is replaced with v_{ds}.

2.3.2. Turbulence estimation

Several methods for isolating the turbulent motions from organized wave motion have been used earlier, each having different weaknesses and no perfect method exists except for regular laboratory waves (Scott et al., 2005; Aagaard and Hughes, 2010). In this study, both the frequency cut-off (e.g. Mocke, 2001; Scott et al., 2005; Foster et al., 2006) and velocity-differencing methods (cf. Feddersen and Williams, 2007) were initially applied. However, as a comparison of the two methods showed qualitatively similar vertical variations in turbulence intensity and intra-wave variations, we present here only the results from the frequency cut-off method.

In this method, the frequency that separates the time scales dominated by wave orbital motion from those dominated by turbulence was determined based on the cross-spectral phase between *u* and *w*, and a high-pass filter was then applied in order to isolate the turbulent velocities. When wave orbital motions dominate the velocity signal, a *u*/*w*-phase of $\pm\pi/2$ is expected with a relatively high coherence; Fig. 4 illustrates an example of the procedure. For this example, a cut-off frequency of 0.6 Hz was selected since that is the highest frequency where the phase is maintained close to $-\pi/2$ (dashed line). At higher frequencies, the phase is constantly fluctuating between $\pm\pi$ and coherence is low. Fig. 5 shows the distribution of selected cut-off frequencies for each ADV at both the intertidal and subtidal rigs. In general, the cut-off frequencies were higher at the intertidal rig compared to the subtidal rig. This would be expected due to smaller water depths at the intertidal rig and thereby smaller turbulent length scales (cf. e.g. Ting and Kirby, 1995).

The calculated turbulent velocities (u', v', w') were combined to yield the turbulent kinetic energy:

$$TKE = \frac{1}{2}\left(\overline{u'^2} + \overline{v'^2} + \overline{w'^2}\right) \quad (3)$$

where overbars denote the average over a 30 min time series. *TKE* can

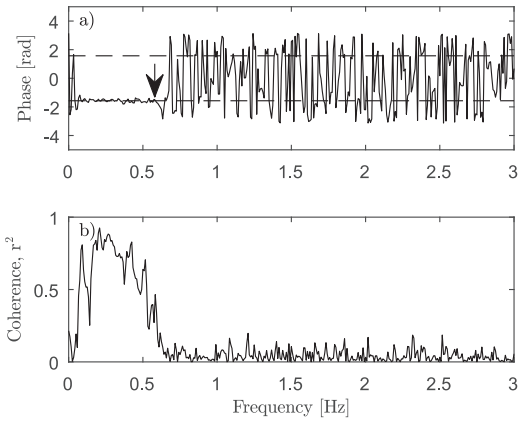

Fig. 4. Example of cross-spectral analysis of cross-shore (*u*) and vertical velocity (*w*) from September 18, 6 a.m. at the subtidal rig. a) The phase, and b) the coherence squared. Horizontal dashed lines in a) mark a phase of $\pm\pi/2$. The arrow indicates the transition from dominance of wave orbital motion to turbulence.

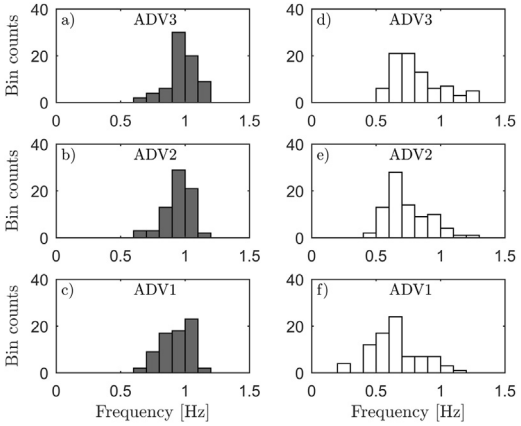

Fig. 5. The applied frequencies for separating orbital wave motion from turbulence. Bin counts on the y-axes and frequencies in intervals of 0.1 Hz on the x-axes. Panel a-c) intertidal rig and panel d-f) subtidal rig.

subsequently be Froude-scaled (*k*):

$$k = \sqrt{TKE/gh} \quad (4)$$

where *g* is the gravitational acceleration and *h* is water depth.

2.3.3. Intra-wave variation of TKE

In order to study *TKE* at an intra-wave time scale, phase-averages of instantaneous *u* and *TKE* were calculated. Individual waves in the velocity time series (ADV3) were identified by use of a zero-down crossing analysis: First, the time series were detrended to remove any long-term trends (e.g. tide), and also high- and low pass filtering ($f = 0.05$ Hz and $f = 0.5$ Hz) were applied in order to remove infragravity wave frequencies and high-frequency noise in the determination of the zero-crossings. Cross-shore orbital velocity at the upper ADV (ADV3) and *TKE* at the three vertical ADV-positions were extracted and normalized against relative wave-phase, *t*/*T*, and then phase-averaged. Each wave was divided into 20 ensembles, and averaging was conducted for a period of 30 min corresponding to one data burst. Between 225 and 494 individual waves were included in the averaging of each record.

In order to examine the phase-lags between cross-shore orbital velocity and *TKE(t)*-maxima at different elevations and for all records, $u(t)$ and *TKE(t)* were cross-correlated. Only examples where cross-correlation coefficients were statistically significant at 95% confidence level were included and the results were grouped according to relative wave height (H_s/h = 0.1–0.2, 0.2–0.3 etc.). Relative wave height classes containing less than 5 time series were disregarded.

2.4. Wave and seabed conditions

The dominant wave types at the two rigs were predicted based on relative wave heights (H_s/h), the wave shape skewness (*SK*) and asymmetry (*AS*), and the local Iribarren numbers (ξ). Based on Ruessink (2010) and Splinter et al. (2011), a threshold between wave shoaling and initial wave breaking was defined as $H_s/h = 0.3$, while the boundary between initial wave breaking and fully breaking conditions was defined as $H_s/h = 0.5$. Fully breaking conditions typically corresponds to surf bores in the inner surf zone. Furthermore, following Grasso et al. (2012), the wave shape skewness (*SK*)/asymmetry (*AS*) ratio can be used to separate dominantly breaking wave conditions (outer surf zone) from surf bore conditions (inner surf zone), with $SK > |AS|$ indicating breaking waves while $SK < |AS|$ indicates surf bores. Wave shape skewness can be calculated as:

$$SK = \frac{\overline{\eta_{inc}^3}}{\left(\overline{\eta_{inc}^2}\right)^{3/2}} \quad (5)$$

where η is the water surface elevation and the subscript *inc* indicates that the time series are high-pass filtered ($f = 0.05$ Hz) in order to isolate the incident short-wave frequencies. For calculation of the shape asymmetry, η is replaced by its Hilbert transform ($\mathscr{H}$):

$$AS = \frac{\overline{\mathscr{H}(\eta_{inc})^3}}{(\overline{\eta_{inc}^2})^{3/2}} \tag{6}$$

The dominant breaker type ($0.3 < H_s/h < 0.5$ and $SK > |AS|$) can be numerically approximated by the local Iribarren number (ξ) (Battjes, 1974):

$$\xi = \frac{\tan\beta}{\sqrt{H_b/L_0}} \tag{7}$$

where β is the slope of the bed, H_b is the wave height at the breakpoint and L_0 is the deep-water wave length (Battjes, 1974). The significant wave period (T_s), which was used to compute L_0, was determined from the zero-th and second moments of the wave spectrum ($(m_0/m_2)^{1/2}$). Based on Battjes (1974) $\xi = 0.4$ was used as the boundary between spilling and plunging breakers.

The bed state changes with the wave and current conditions, and it can be roughly characterised using the mobility number which is an implicit expression for the bed shear stress:

$$\Psi = \frac{u_s^2}{(s-1)gD} \tag{8}$$

where u_s is the significant wave orbital velocity, s is the ratio of sediment and water density ($= 2.65$), and D is the mean grain size. According to Dingler and Inman (1976), vortex ripples are present for $\Psi < 40$ while low post-vortex ripples dominate for $40 < \Psi < 240$ and flat bed prevails for $\Psi > 240$. Wave ripple geometry was moreover identified from bed profile scans. Ripple heights were determined by $\eta_r = 2\sqrt{2}\sigma_r$, where σ_r is the standard deviation of the bed elevation. Ripple wavelengths (λ) were identified using the peak in the autocorrelation function of individual bed profiles.

3. Results

3.1. Experimental conditions

Between September 17 and September 25, H_s at the positions of the two rigs varied between approximately 0.2 m and 0.65 m, with the largest wave heights occurring towards the end of the period (Fig. 6b). During the first six days, swell conditions prevailed with a peak spectral wave period of about 12 s, hereafter, the conditions changed to a dominance of wind waves with a peak period of about 5 s (Fig. 6c).

The wave spectra were however rather broad-banded (Fig. 7) and both swell and short-waves coexisted in the beginning and the end of the period. Especially on September 21 and 22 well-developed harmonics are noticeable. The wave spectra are only shown for the subtidal rig due to many data gaps at the intertidal rig as no data was obtained during low tide.

At the positions of both rigs, the local bed slope was initially $\beta = 0.037$. Between September 19 and 22, sediment was transported onshore causing erosion at the seaward slope of the intertidal bar and thus at the positions of both rigs, while the intertidal bar accreted in the vertical and the seaward slope increased (Fig. 2). On the 25th of September, sediment was eroded from the upper part of the intertidal bar while deposition occurred lower down on the seaward slope, particularly at the location of the subtidal rig, where instruments were buried.

Visual observations during the campaign indicated that the main breakpoint was often located in between the two rigs during large parts of the tide. This is consistent with theoretical considerations. Based on the relative wave heights and the *SK/AS*-ratio, waves were predicted to be mainly shoaling and breaking at the subtidal rig, while surf bores dominated at the position of the intertidal rig (Fig. 8a). Even for $0.3 < H_s/h < 0.5$ the waves at the intertidal rig were in most cases strongly asymmetric ($SK < |AS|$) and therefore classified as surf bores. The initially breaking waves were predicted to be predominantly of the spilling type (Fig. 8b).

The higher percentage of broken waves at the intertidal rig was also expressed by the strength of the mean cross-shore current (U) with near-bed velocities being up to a factor 2–3 larger at the intertidal rig compared to the subtidal rig (Fig. 9a). At the upper elevation (ADV3), the difference in current velocity between the intertidal and subtidal rig was smaller (Fig. 9b). This is probably a result of the lack of ADV3 measurements at the intertidal rig at lower tidal stages when U tended to be largest (Fig. 6d). Occasionally, positive near-bed (ADV1) current velocities occurred at the subtidal rig (Fig. 9a). This was at times when the instrument elevation (z) was less than 0.04 m, suggesting that ADV1 may at times have been within the wave boundary layer with onshore mean flows perhaps due to boundary layer streaming.

The different wave and current conditions at the two rigs find expression in the bed states. Based on the values for Ψ during the first week of the campaign, low post-vortex ripples were present at the subtidal rig, while flat beds as well as low post-vortex ripples probably dominated at the intertidal rig (Fig. 8a). This is consistent with field observations and preliminary examination of the sonar records from both the intertidal and the subtidal rigs (see Brinkkemper et al., 2017b). The height of the post-vortex ripples was typically $\eta_r = 0.01$–0.025 m, while the ripple wavelength (λ) was mostly in the range $\lambda = 0.07$–0.2 m corresponding to approximately 0.1 d_0, where d_0 is the wave orbital diameter. This indicates that the post-vortex ripples were of the anorbital type (cf. Wiberg and Harris, 1994).

3.1.1. Time-averaged turbulence levels at the intertidal and subtidal rigs

The different wave conditions and bed states at the intertidal and subtidal rigs are expected to affect turbulence generation and intensity. The time-averaged Froude-scaled *TKE* (k) correlated positively with the relative wave height (Fig. 10). For shoaling waves ($H_s/h < 0.3$) the relationship is likely due to the fact that larger waves and orbital velocities in shallower water result in increased friction at the bed and thereby more intense generation of turbulent eddies. For breaking waves ($H_s/h > 0.3$) where surface-generated turbulence is introduced, larger amounts of turbulence are expected to reach the bed when H_s/h is large. This explains the positive correlation between k and H_s/h for both shoaling and breaking waves.

Comparing the turbulence levels at the intertidal and subtidal rigs (Fig. 10), it appears that for shoaling and breaking waves ($H_s/h < 0.5$) k was larger at the subtidal rig. This is probably a result of larger H_s for similar H_s/h due to the larger water depths at the subtidal rig compared to the intertidal rig. Moreover, the higher elevation of ADV3 at the subtidal rig (initially $z_{ADV3} = 0.50$ m at the subtidal rig and $z_{ADV3} = 0.39$ m at the intertidal rig) might have contributed to higher turbulence intensities.

To examine the vertical structure of the turbulence, class-averaging of k based on the relative wave heights has been applied (Fig. 11). The water column appears well mixed with no statistically significant vertical differences in k. There is, however, a slight increase in k at higher elevations indicating a turbulence source at the top of the water column, and, especially for the intertidal rig, an increase in k towards the bed, indicating the presence of bed-generated turbulence.

3.1.2. Intra-wave turbulence intensity

Time-averaged turbulence intensity strongly affects the magnitude of suspended sediment concentrations (e.g. Beach and Sternberg, 1996; Aagaard and Jensen, 2013; van der Zanden et al., 2017), but intra-wave variations in *TKE* might also be of importance for the magnitude and direction of the short-wave sediment transport rate as it affects when in the wave phase the highest concentrations occur. Four representative examples of $u(t)$ and $TKE(t)$ for different wave types are given in Fig. 12. Note, that *TKE*-levels have been normalized with respect to

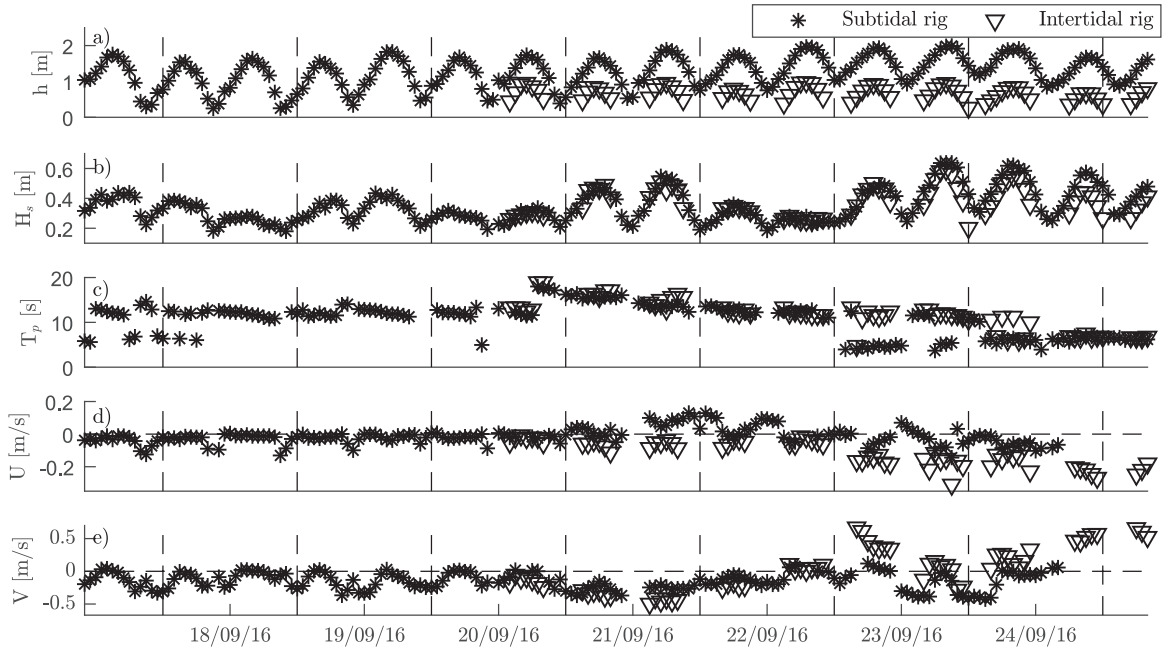

Fig. 6. a) Water depth (h), b) significant wave height (H_s), c) peak wave period (T_p), d) mean cross-shore current velocity (U_{ADV1}) and e) mean longshore current velocity (V_{ADV1}) at the positions of the two rigs from September 17–25, 2016. Measurements from the intertidal and subtidal rigs are represented by triangles and asterisks, respectively.

maximum *TKE* at the upper sensor (ADV3) in order to emphasize intra-wave and vertical variations.

For shoaling waves ($H_s/h = 0.2$ and ($SK > |AS|$), *TKE(t)* was typically largest near the bed (Fig. 12a). Intra-wave variations were small, but maximum *TKE(t)* occurred beneath the wave crest ($t/T = 0.825$). Friction between the wave orbital flow and the bed is probably the main turbulence source, i.e. *TKE(t)* peaks when *u(t)* is maximum. Hence, there is no evidence of bed form-induced time lags between *u(t)* and *TKE(t)*, but since ripples were small and of the anorbital type (Fig. 8a), this is not unexpected.

For spilling breakers ($H_s/h = 0.3$, $SK > |AS|$), *TKE(t)* at ADV3 typically peaked just after the maximum orbital velocity, whereas *TKE(t)* was small at ADV2 with little temporal structure (Fig. 12b). Closer to the bed (ADV1), *TKE(t)* often had a broad maximum under the wave trough. These variations in the vertical suggest that there were two sources of turbulence: surface- and bed-generated. In the upper part of the water column (ADV3), the timing of the turbulence beneath the wave crest is consistent with turbulence production near the crest of spilling breakers and slow downward propagation of eddies. Near the bed (ADV1), offshore-directed mean currents (Fig. 9) probably increased the bed shear stress during the offshore wave phase, and thereby caused a low and broad *TKE(t)* maximum beneath the wave trough.

For weak surf bores with $H_s/h = 0.3$ (Fig. 12c), *TKE(t)* was largest near the bed (ADV1). In the upper part of the water column (ADV2 and ADV3), *TKE(t)* shows no distinct variations perhaps due to lack of penetration of surface-generated turbulence due to the sensor levels. In contrast, near the bed (ADV1) *TKE(t)* peaked at the wave front ($t/T = 0.475$). As the undertow was weak for this example (-0.04 m/s), the increase in *TKE(t)* at this wave phase is probably not related to current shear, as suggested for the spilling wave case, but instead perhaps a result of velocity asymmetry. The acceleration (du/dt) is largest at the wave front and causes evolution of a thin wave boundary layer at this wave phase. This is expected to increase the friction-induced

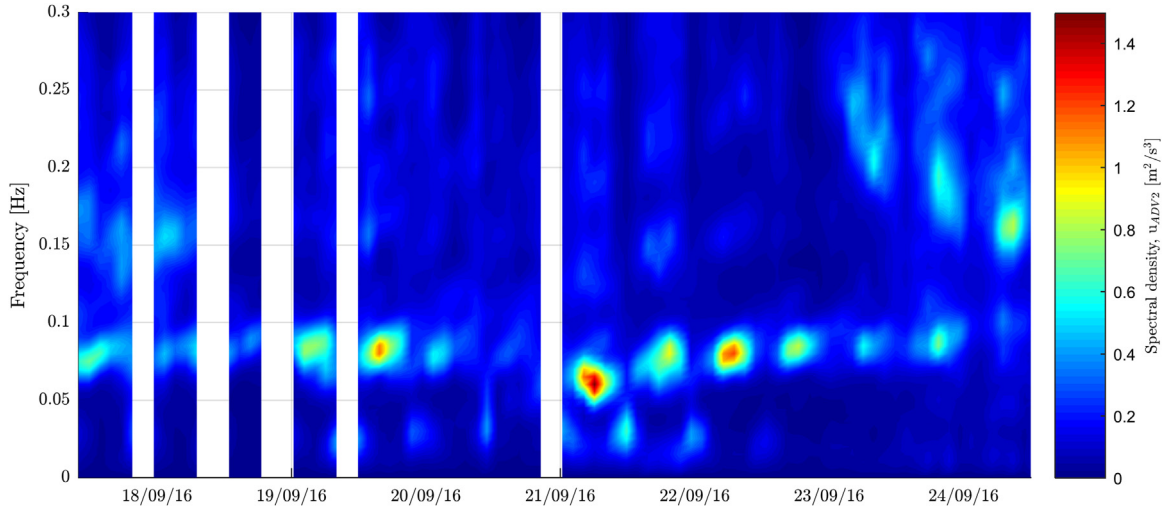

Fig. 7. Wave-energy spectra (u_{ADV2}) at the subtidal rig.

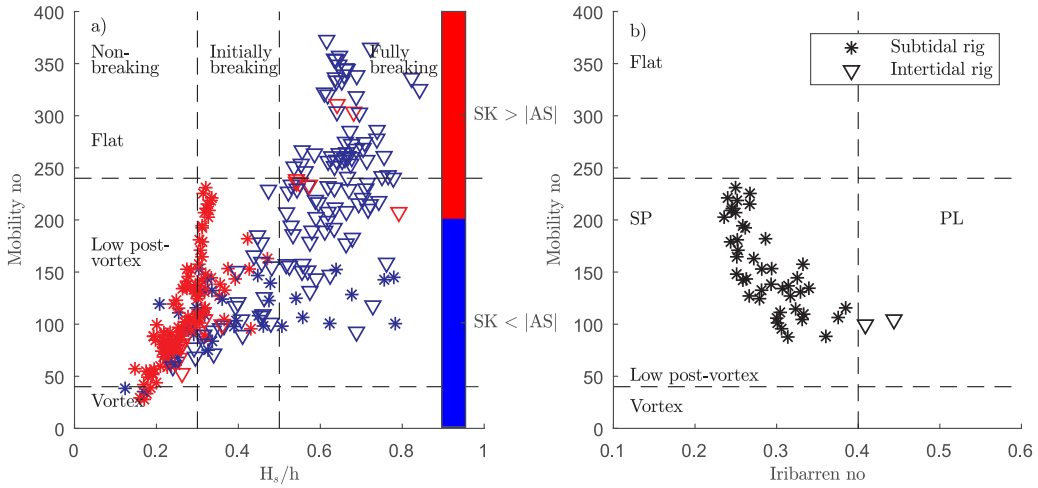

Fig. 8. a) Mobility number (Ψ) versus relative wave height (H_s/h) at the intertidal (triangles) and subtidal (asterisks) rig. The vertical dashed lines indicate the approximate boundary between shoaling, initially breaking and fully breaking waves (H_s/h = 0.3/0.5). Horizontal dashed lines indicate the boundaries between vortex ripples (Ψ < 40), low post-vortex ripples (40 < Ψ < 240) and flat bed conditions (Ψ > 240) (cf. Dingler and Inman, 1976). The colours separate dominantly breaking wave conditions (red) from surf bores (blue) based on the ratio of wave skewness (*SK*) and asymmetry (*AS*) (cf. Grasso et al., 2012). b) Mobility number (Ψ) versus Iribarren number (ξ) for time series with H_s/h = 0.3–0.5 and $SK > |AS|$ at the intertidal (triangles) and subtidal (asterisks) rig. Vertical dashed line indicates the theoretical boundary between spilling (SP) and plunging (PL) breakers (cf. Battjes, 1974).

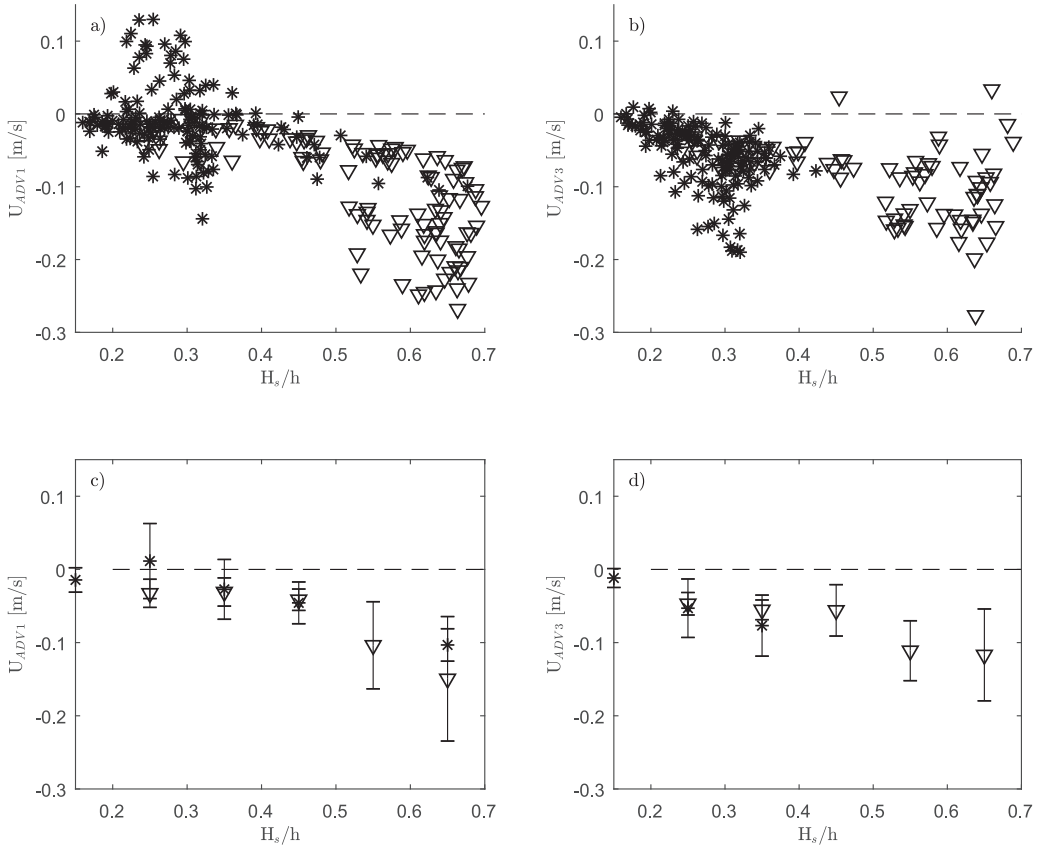

Fig. 9. a-b) Mean cross-shore current velocity (*U*) versus relative wave height (H_s/h) at a) the near-bed ADV1 and b) upper ADV3. c-d) Bin means of mean cross-shore current velocity at c) the near-bed ADV1 and d) upper ADV3. The vertical lines are ± one standard deviation. Measurements from the intertidal and subtidal rigs are represented by triangles and asterisks, respectively.

turbulence.

For strong surf bores with H_s/h= 0.65 (Fig. 12d), turbulence intensities were largest in the upper part of the water column (ADV3). Maximum *TKE(t)* occurred at the wave front (t/T = 0.475). *TKE(t)* peaked first at the upper velocity sensor (ADV3) and subsequently at the lower sensors but with less temporal structure. This suggests downward penetration of surface-induced turbulence.

To examine more generally the trends in the phasing of $TKE(t)_{max}$, class-averaged lags of *TKE(t)* relative to maximum onshore velocity under the wave crest are presented in Fig. 13. Beneath shoaling waves of small relative wave heights (H_s/h < 0.2), near-bed *TKE(t)* (ADV1) peaked beneath the wave crest (maximum orbital velocities) due to bed

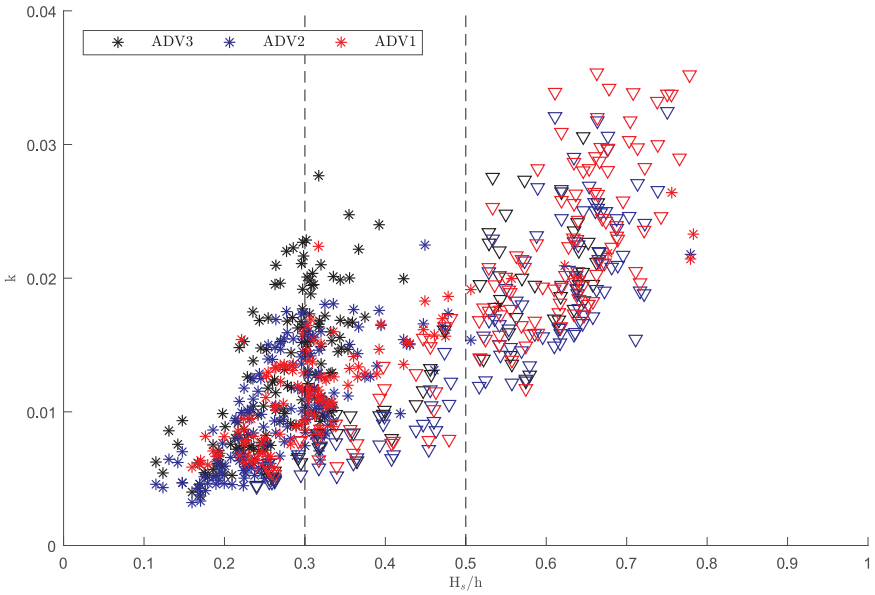

Fig. 10. Froude-scaled *TKE* (*k*) versus relative wave height (H_s/h) at the intertidal (triangles) and subtidal rig (asterisks), respectively. Near-bed measurements, ADV1 (lower sensor), are presented in red, ADV2 (middle sensor) in blue, and ADV3 (upper sensor) in black. The vertical dashed lines indicate the boundaries between shoaling and initially breaking waves ($H_s/h = 0.3$) and initially breaking and fully breaking conditions ($H_s/h = 0.5$).

friction with no discernible bed form effects on the *TKE(t)*-phasing. For $H_s/h = 0.2$–0.3 the timing of *TKE(t)* at ADV2 and ADV3 indicates incipient wave breaking (i.e. maximum *TKE(t)* after the wave crest) at the subtidal rig which resulted in increased mean current velocities (Fig. 9d). Current shear probably increased *TKE(t)* beneath the wave trough as indicated in Fig. 12b. The large standard deviation of $TKE(t)_{max,ADV1}$ implies maximum *TKE(t)* over the entire trough to crest phase. This is likely be due to broad velocity spectra (e.g. Fig. 7): pure shoaling dominated in some time series resulting in maximum *TKE(t)* beneath the wave crest (Fig. 12a), while occasional wave breaking in other time series caused maximum *TKE(t)* beneath the wave trough (Fig. 12b). For spilling breakers ($H_s/h = 0.3$–0.4, the subtidal rig), the trend was similar and surface-induced turbulence beneath the wave crest (ADV3/2) did not penetrate to the bed (ADV1).

Beneath surf bores at the intertidal rig ($SK < |AS|$ and $H_s/h > 0.3$), *TKE(t)* peaked at the wave front ((t/T = -0.2 to -0.3) without significant

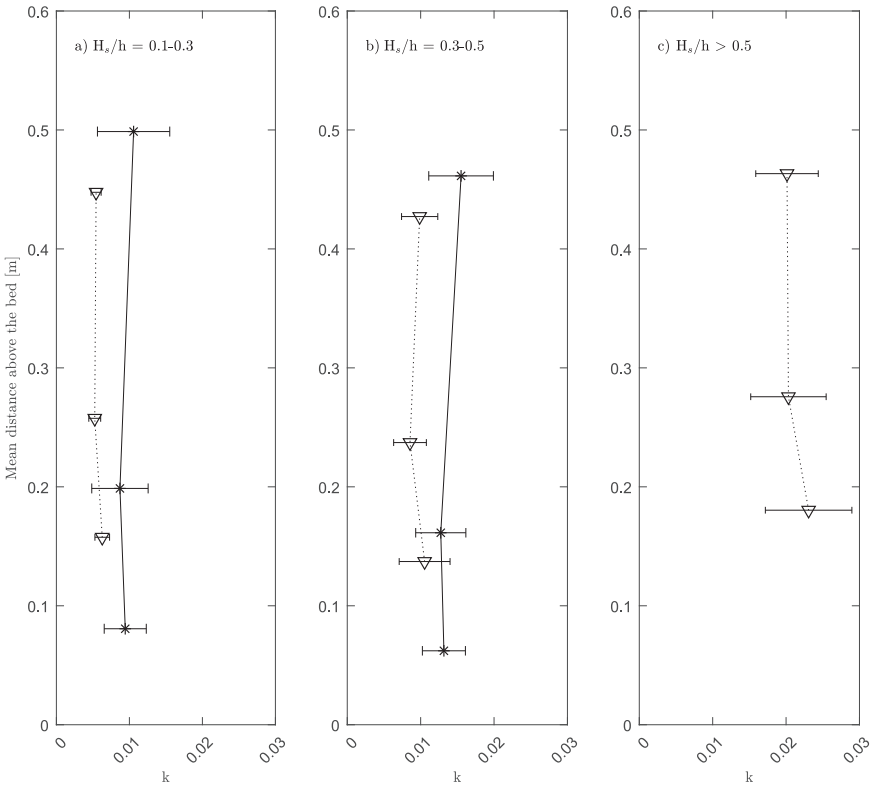

Fig. 11. Vertical structure of Froude-scaled *TKE* (*k*) for relative wave heights (H_s/h) a) $H_s/h = 0.1$–0.3, b) $H_s/h = 0.3$–0.5 and c) $H_s/h > 0.5$. Measurements from the intertidal and subtidal rigs are presented by dotted lines with triangles and thin lines with asterisks, respectively. The horizontal lines are ± one standard deviation.

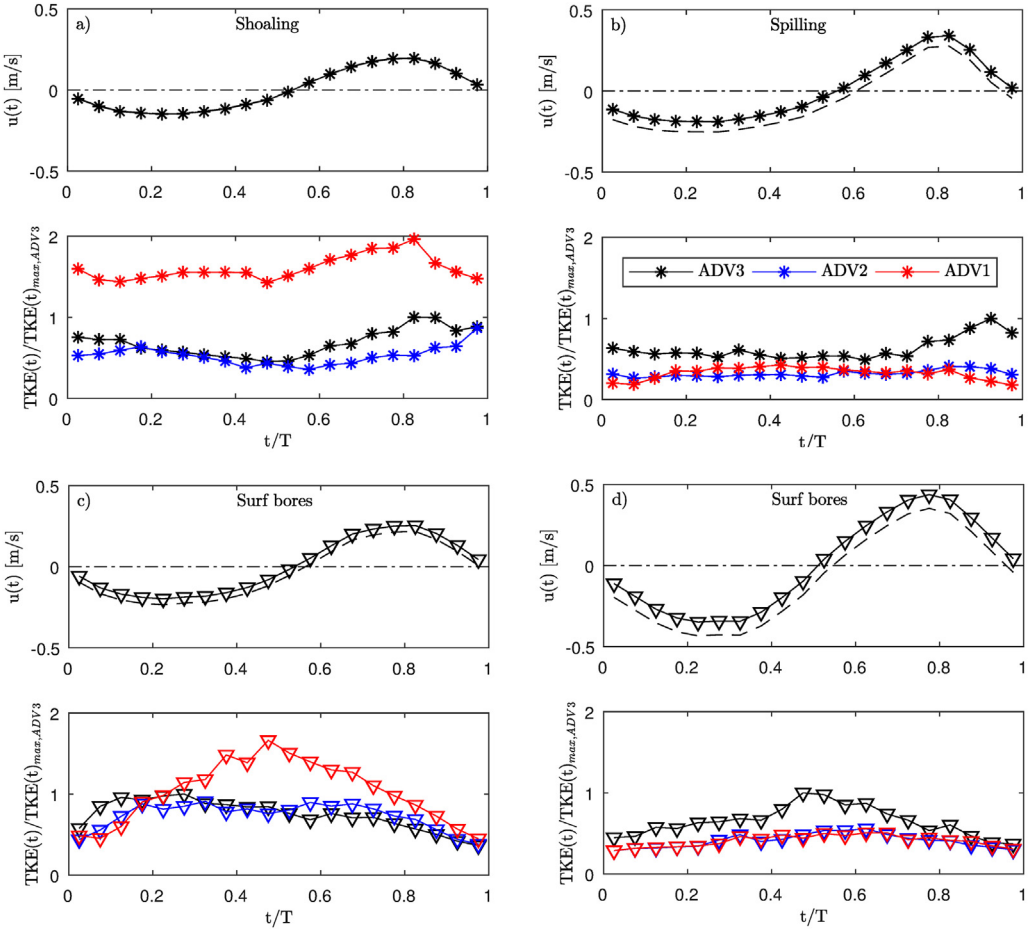

Fig. 12. Phase-averaged cross-shore orbital velocity (u) and normalized *TKE* (with respect to the maximum *TKE* at ADV3). The dashed line is the full cross-shore velocity signal, i.e. including the mean current. a) Shoaling waves (18/09 at 2 p.m.), $H_s/h = 0.2$ & $SK > |AS|$, b) Spilling breakers (20/09 at 12 a.m.), $H_s/h = 0.3$ & $SK > |AS|$, c) Surf bores (20/09 at 4.30 p.m.), $H_s/h = 0.3$ & $SK < |AS|$ and d) Surf bores (23/09 at 6.30 p.m.), $H_s/h = 0.65$ & $SK < |AS|$. Normalized *TKE* at the three vertical positions are shown (ADV1: red, ADV2: blue and ADV3: black). Measurements from the intertidal and subtidal rigs are represented by triangles and asterisks, respectively. (For interpretation of the references to color in this figure legend, the reader is referred to the web version of this article).

vertical variation (Fig. 13a). Despite the similar *TKE(t)*-phasing, two sources of turbulence very likely existed as the vertical variation in k (Fig. 11) indicated an increase in k-levels towards both higher elevation and the bed. Hence, turbulence was injected at the surface (Fig. 12d) but there was also a contribution from bed friction (Fig. 12c) possibly associated with fluid acceleration which was large at this wave phase (Table 1).

To summarize, the intra-wave variability of *TKE(t)* beneath shoaling waves, spilling breakers and surf bores showed that near-bed *TKE(t)* (ADV1) was phase-coupled to the orbital velocity ($u(t)$) beneath shoaling waves and mainly generated by bed friction, while breaking waves increased offshore-directed mean current velocities resulting in increased shear beneath the wave trough. For surf bores, acceleration skewness and penetration of surface-induced turbulence were both likely causes for maximum near-bed *TKE(t)* at the wave front. Higher in the water column (ADV2/3), turbulence generated by spilling breakers peaked just after the wave crest. Beneath surf bores the vertical mixing was larger (no significant time lag between ADV3 and ADV2), and the turbulent wave front caused maximum *TKE(t)* close to the zero-up crossing.

4. Discussion

4.1. Applied methods and time-averaged turbulence intensity

In order to estimate the turbulent kinetic energy (*TKE*) using the frequency cut-off method, it was necessary to identify the frequencies that separated orbital from turbulent motions. This was done visually, based on the phase between u and w. In some cases, the transition away from a phase of $\pi/2$, i.e. orbital dominated motion, was not very distinct, and at times it is less than straightforward to determine the most appropriate cut-off frequency. This was especially the case for the lowest ADVs (ADV1). Scott et al. (2005) examined the sensitivity of *TKE* magnitude to the selected frequency cut-off and found that increasing the cut-off frequency by a factor two caused a 40% reduction in *TKE*. Based hereon, we estimate a potential error of 10–20% in the *TKE* estimates in this study.

The turbulence intensities, estimated using the frequency cut-off method, were also compared to calculations based on the velocity-differencing method (Feddersen and Williams, 2007). The comparison showed that the velocity-differencing method resulted in Froude-scaled *TKE* (k) that were about a factor two larger than the results of the frequency cut-off method, which is in accordance with previous work (Scott et al., 2005; Yoon and Cox, 2010). The results from the above mentioned sensitivity analyses by Scott et al. (2005) imply that in order to obtain the same k magnitudes from the two methods, the cut-off frequency would typically have to be lowered well within the wind wave frequency band for the subtidal rig (Fig. 5). However, what is probably more important, the vertical k-profiles and the intra-wave variabilities were qualitatively similar for the two methods, and thus our results would appear to be robust despite the uncertainty on determination of the cut-off frequencies and the ensuing absolute k-

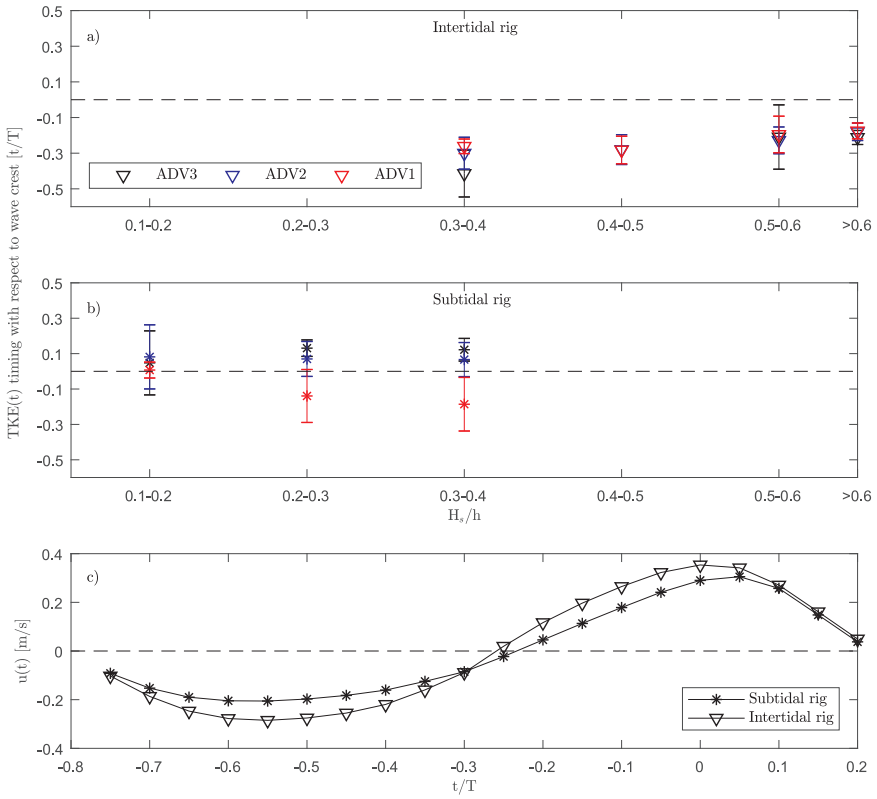

Fig. 13. Mean values of the significant (95% confidence interval) timing of maximum *TKE(t)* with respect to the wave crest (max $u(t)$) for different classes of relative wave heights ($H_s/h = 0.1–0.2$, 0.2–0.3 etc.). The vertical lines are ± one standard deviation. Positive lag indicates that *TKE(t)* was maximum after passing of the wave crest. Measurements from ADV1 are shown in red, ADV2 in blue and ADV3 in black. The lower plot, c), shows the average horizontal orbital velocity ($u(t)$). Measurements from the intertidal and subtidal rig are represented by triangles and asterisks, respectively.

Table 1
Means of maximum acceleration and its phasing for different H_s/h-bins ($H_s/h = 0.1–0.2$, $H_s/h = 0.2–0.3$ etc.) at the intertidal and subtidal rig.

	H_s/h = 0.1–0.2	H_s/h = 0.2–0.3	H_s/h = 0.3–0.4	H_s/h = 0.4–0.5	H_s/h = 0.5–0.6	H_s/h > 0.6
Mean of maximum du/dt [m/s^2]						
Intertidal rig			1.8	2.8	2.4	2.7
Subtidal rig	1.2	1.5	1.9			
Mean timing (t/T) **of maximum** du/dt						
Intertidal rig			− 0.20	− 0.23	− 0.14	− 0.22
Subtidal rig	− 0.16	− 0.03	− 0.12			

values. Visual examination of the calculated intra-wave variabilities in *TKE* moreover revealed qualitatively similar variations within a relative wave height bin. This gives confidence in the interpretation of how turbulence intensity varied in time and with depth, even though the broad wave spectra of the time series lead to large temporal variability in the waves incorporated in the phase-averaging.

The overall magnitude of k within the water column is generally consistent with previous studies. Under spilling breakers at the subtidal rig ($H_s/h = 0.3–0.5$), k was about 0.015 (Fig. 11) while Ting and Kirby (1994) observed k in the range of 0.03–0.05 beneath spilling breakers just onshore of the main breakpoint. The larger k is probably related to the fact that those results were obtained beneath regular waves in a wave tank, rather than beneath irregular waves in the field. Scott et al. (2005), for example, observed larger turbulence intensities beneath regular waves than beneath irregular waves. Under surf bores at the intertidal rig ($H_s/h > 0.3$), our estimates of k were in the order of 0.01–0.02 (Fig. 11) which is in general agreement with the magnitudes of 0.015–0.04 reported by Ruessink (2010). Ruessink (2010) moreover showed a tendency towards an exponential increase in cross-shore Reynolds stress with increasing H_s/h. This is consistent with our findings on the relation between k and H_s/h (Fig. 10). Fig. 10 moreover showed that for similar H_s/h, k was larger at the subtidal rig compared to the intertidal rig. This emphasizes the importance of measuring turbulence at more cross-shore locations in order to examine cross-shore variability in turbulence characteristics and not only relating the characteristics to H_s/h.

The water column appeared well mixed as there was no significant vertical variation in k, which is consistent with field observations by Ruessink (2010). Still, there were indications of an increase in k near the bed at the intertidal rig suggesting bed-generated turbulence. At the subtidal rig, *TKE(t)* peaked earlier near the bed than higher in the water column for shoaling waves ($H_s/h < 0.3$) also indicating a turbulence source at the seabed. An increase in k towards the seabed is in agreement with observations by Brinkkemper et al. (2016).

4.2. Intra-wave turbulence intensity

The intra-wave analysis showed that *TKE(t)* peaked beneath the wave crest for $H_s/h < 0.2$, rather than at zero-crossings which might have been expected if vortex ripples had been present (e.g. van der Werf et al., 2007). However, for the present measurements, ripples in the shoaling wave zone were predicted (and observed) to be of the post-

vortex/anorbital type (Fig. 8a). Hence, while *TKE* was mainly bed-generated, we observed no influence of bed forms on the timing of *TKE* production.

For breaking waves ($0.3 < H_s/h < 0.5$ at the subtidal rig), the vertical profiles of k resembled those for shoaling wave conditions except for a more prominent increase in the upper part of the array, as expected, because of surface-injected *TKE*. The earlier injection of turbulence near the bed (ADV1) compared to elevations higher in the water column (ADV2/3) (Fig. 13b) again implies that turbulence was generated at the bed despite the lack of significant variation in k between ADV2 and ADV1 (Fig. 11). Regardless of the qualitatively similar vertical profiles for shoaling and breaking wave conditions, the near-bed increase in *TKE* was probably caused by different processes. For shoaling waves of small relative wave heights ($H_s/h < 0.2$), friction between the moving fluid and the bed probably was the main turbulence source, while as wave breaking commenced (in some cases already for $H_s/h = 0.2$–0.3), mean offshore-directed current velocities very likely reinforced the near-bed turbulence. The breaker type was observed (and predicted: Fig. 8b) to be mainly of the spilling type, and the vertical profile of k indicates that significant amounts of surface-induced turbulence rarely reached the seabed, consistent with previous laboratory work beneath spilling breakers (Ting and Kirby, 1996). Intra-wave analyses beneath spilling breakers at the subtidal rig showed that in the mid-upper parts of the water column (ADV2/3), *TKE(t)* was maximum immediately after the wave crest (Fig. 13b, lag = 0.1 t/T). This is consistent with laboratory observations under spilling waves by Ting and Kirby (1994) and Govender et al. (2002). Near the bed, however, the mean time lag of *TKE(t)* showed maximum *TKE(t)* near the zero-up crossing which indicates that the turbulence had a different origin. The timing of the *TKE(t)*-maximum is consistent with vortex ejections from wave ripples, but ripples were of the post-vortex type and likely even smaller than for the shoaling wave case. Visual examination of the phase-averages instead suggested that the mean phasing was an artefact of the averaging procedure. In fact $TKE(t)_{ADV1}$ showed either a low and broad peak beneath the wave trough (Fig. 12b) or a peak close to the wave crest (Fig. 12a). In addition, some scatter in the $TKE(t)_{ADV1}$-phasing is expected due to the broadness of the peaks (Fig. 12b) which make the cross-correlation analyses less clear. Laboratory experiments have also shown an effect of current shear on turbulence production. Ruessink et al. (2011) observed larger k-levels beneath the wave trough compared to the crest when superimposing a countercurrent ($U = -0.4$ m/s) on an asymmetric oscillatory flow.

For surf bores at the intertidal rig ($SK < |AS|$), *TKE(t)* peaked about the timing of zero-up crossing (Fig. 12c, d and Fig. 13a) which coincides with the arrival of the bore front. For strong surf bores, this timing was very likely a result of turbulence induced by the surface-roller consistent with observations by Butt et al. (2004). For weak surf bores, surface-induced turbulence did not appear to reach the seabed (Fig. 12c). Instead, friction-induced turbulence peaked near the zero-up crossing, possibly as a result of the large fluid acceleration at this wave phase (Table 1). Accordingly, Nielsen (2006) showed, based on laboratory data, that beneath acceleration skewed waves the wave boundary layer only has short time to develop until maximum velocity is achieved, whence the layer is relatively thin and the shear stress large.

5. Conclusions

The present field data set was obtained at two instrument rigs located on the upper and lower seaward slopes of a shallow, longshore bar. At the intertidal rig, surf bores prevailed (when the station was submerged) and the bed was typically flat. In contrast, shoaling waves and spilling breakers dominated at the subtidal rig and the bed state was most often composed of low post-vortex ripples of the anorbital type. These different conditions made it possible to investigate turbulence characteristics (intensity, vertical variation and intra-wave variability) for different wave types and bed conditions. The results showed that findings from earlier laboratory experiments (e.g. Ting and Kirby, 1994; Govender et al., 2002; Scott et al., 2005; Shin and Cox, 2006; Brinkkemper et al., 2016) in many respects correspond with field observations. However, turbulence production beneath different wave types was shown to be complex both in time and space. Hence, turbulence was not only generated by wave breaking and bed friction: opposing mean currents and acceleration skewness also appeared to play a part.

In the upper part of the water column (ADV2/3) turbulence was injected by the wave breaking process. Beneath spilling breakers, *TKE(t)* was maximum just after the wave crest, while surf bores induced turbulence at the bore front (i.e. near zero-up crossing). Near the bed (ADV1), *TKE(t)* was phase-coupled to the orbital velocity (u) for shoaling waves suggesting that the turbulence was generated by bed friction. The lack of phase-shifts indicates that the bed forms developed in the fine-grained sand did not systematically affect the turbulence ejection from the bed. For spilling breakers, $TKE(t)_{ADV1}$ was maximum close to the off- to onshore flow reversal likely due to increased bed shear stress under wave troughs caused by wave-current interaction. Beneath surf bores, $TKE(t)_{ADV1}$ peaked at the wave front which might be a result of both acceleration skewness and occasionally penetration of surface-induced turbulence to the bed.

Acknowledgements

The present work was funded by The Danish Council For Independent Research (grant no. 4181-00045) and University of Copenhagen. J. Brinkkemper and G. Ruessink were funded by the Dutch Technology Foundation STW, which is part of the Netherlands Organization for Scientific Research (NWO), and is partly funded by the Ministry of Economic Affairs (project number 12397). We would like to acknowledge The Danish Coastal Authorities for access to offshore wave data, and we wish to thank Vera van Bergeijk, Johnny van de Wetering, Ivo Naus, Timothy Price, Marcel van Maarseveen, Henk Markies, Verner B. Ernstsen, Mathias Madsen, Per Freiberg, and Paul Christiansen for their assistance in the field.

References

Aagaard, T., Hughes, M.G., 2010. Breaker vortices and sediment suspension in the surf zone. Mar. Geol. 271, 250–259.
Aagaard, T., Hughes, M.G., 2013. Sediment transport. In: In: Shroder, J.A. (Ed.), Treatise On Geomorphology 10. Academic Press, San Diego, pp. 75–105.
Aagaard, T., Jensen, S.G., 2013. Sediment concentration and vertical mixing under breaking waves. Mar. Geol. 336 (146), 159.
Battjes, J.A., 1974. Surf similarity. In: Proceedings of the 14th Coastal Engineering Conference, Am. Soc. Civil Eng., New York, pp. 466–480.
Beach, R.A., Sternberg, R.W., 1996. Suspended-sediment transport in the surf zone: response to breaking waves. Cont. Shelf Res. 16, 1989–2003.
Brinkkemper, J.A., Lanckriet, T., Grasso, F., Puleo, J.A., Ruessink, B.G., 2016. Observations of turbulence within the surf and swash zone of a field-scale sandy laboratory beach. Coast. Eng. 113, 62–72.
Brinkkemper, J.A., de Bakker, A.T.M., Ruessink, B.G., 2017a. Intrawave sand suspension in the shoaling and surf zone of a field-scale laboratory beach. J. Geophys. Res. Earth Surf. 122. https://doi.org/10.1002/2016JF004061.
Brinkkemper, J.A., Christensen, D.F., Price, T., Naus, I., Hansen, A., van Bergeijk, V., van de Wetering, J., Ruessink, B.G., Ernstsen, V.B., Aagaard, T., 2017b. Surf zone morphodynamics during low-moderate energetic conditions; the TASTI field experiment. Proc. Coast. Dyn. 1038–1048.
Butt, T., Russell, P., Puleo, J., Miles, J., Masselink, G., 2004. The influence of bore turbulence on sediment transport in the swash and inner surf zones. Cont. Shelf Res. 24, 757–771.
Dingler, J.R., Inman, D.L., 1976. Wave-formed ripples in nearshore sands. In: Proceedings of the 15th International Conference Coastal Eng. Am. Soc. Civil Eng, New York, pp. 2109–2126.
Elgar, S., Raubenheimer, B., Guza, R.T., 2005. Quality control of acoustic Doppler velocimeter data in the surfzone. Meas. Sci. Technol. 16, 1889–1893.
Emery, W.J., Thomson, R.E., 2001. Data Analysis Methods in Physical Oceanography, 2nd ed. Elsevier, pp. 638.
Feddersen, F., Williams, A.J., 2007. Direct estimation of the reynolds stress vertical structure in the nearshore. J. Atmos. Ocean. Technol. 24, 102–116.
Foster, D.L., Beach, R.A., Holman, R.A., 2006. Turbulence observations of the nearshore

wave bottom boundary layer. J. Geophys. Res. 111, C04011. https://doi.org/10.1029/2004JC002838.
Govender, K., Mocke, G.P., Alport, M.J., 2002. Video-imaged surf zone wave and roller structures and flow fields. J. Geophys. Res. 107 (C7), 3072.
Grasso, F., Castelle, B., Ruessink, B.G., 2012. Turbulence dissipation under breaking waves and bores in a natural surf zone. Cont. Shelf Res. 43, 133–141.
Henderson, S.M., Allen, J.S., Newberger, P.A., 2004. Nearshore sandbar migration predicted by an eddy-diffusive boundary layer model. J. Geophys. Res. 109, C06024. https://doi.org/10.1029/2003JC002137.
Mariño-Tapia, I.J., O'Hare, T.J., Russell, P.E., Davidson, M.A., Huntley, D.A., 2007. Cross-shore sediment transport on natural beaches and its relation to sandbar migration patterns: 2. Appl. Field Transp. Parameter. J. Geophys. Res. 112, CO3002.
Mocke, G.P., 2001. Structure and modeling of surf zone turbulence due to wave breaking. J. Geophys. Res. 106, 17039–17057.
Mori, N., Suzuki, T., Kakuno, S., 2007. Noise of acoustic doppler velocimeter data in bubbly flows. J. Eng. Mech. 133, 122–125.
Nadaoka, K., Hino, M., Koyano, Y., 1989. Structure of the turbulent flow field under breaking waves in the surf zone. J. Fluid Mech. 204, 359–387.
Nichols, C.S., Foster, D.L., 2007. Full-scale observations of wave-induced vortex generation above a rippled bed. J. Geophys. Res. 112, C10015. https://doi.org/10.1029/2006JC003841.
Nielsen, P., 1992. Coastal Bottom Boundary Layers and Sediment Transport (Chapter 3). Advanced Series on Ocean Engineering World Scientific, Singapore (5 Toh Tuck Link, Singapore 596224).
Nielsen, P., 2006. Sheet flow sediment transport under waves with acceleration skewness and boundary layer streaming. Coast. Eng. 53, 749–758. https://doi.org/10.1016/j.coastaleng.2006.03.006.
O'Hara Murray, R.B., Thorne, P.D., Hodgson, D.M., 2011. Intrawave observations of sediment entrainment processes above sand ripples under irregular waves. J. Geophys. Res. 116, C01001. https://doi.org/10.1029/2010JC006216.
Peregrine, D.H., Svendsen, I.A., 1978. Spilling breakers, bores and hydraulic jumps. In: Proceedings of the 16th International Conference Coastal Engineering, pp. 540–550.
Ruessink, B.G., 2010. Observation of turbulence within a natural surf zone. J. Phys. Oceanogr. 40, 2696–2712.
Ruessink, B.G., Michallet, H., Abreu, T., Sancho, F., van der A, D.A., van der Werf, J.J., Silva, P.A., 2011. Observations of velocities, sand concentrations, and fluxes under velocity-asymmetric oscillatory flows. J. Geophys. Res. 116, C03004. https://doi.org/10.1029/2010JC006443.
Ruessink, B.G., Kuriyama, Y., 2008. Numerical predictability experiments of cross-shore sandbar migration. Geophys. Res. Lett. 35, L01603. https://doi.org/10.1029/2007GL032530.
Scott, C.P., Cox, D.T., Maddux, T.B., Long, J.W., 2005. Large-scale laboratory observations of turbulence on a fixed barred beach. Meas. Sci. Technol. 16, 1903–1912.
Scott, N.V., Hsu, T.-J., Cox, D., 2009. Steep wave, turbulence, and sediment concentration statistics beneath a breaking wave field and their implications for sediment transport. Cont. Shelf Res. 29, 2303–2317.
Shepard, F.P., 1950. Beach Cycles in Southern California. US Army Corps of Engineers, Beach Erosion Board, Tech, Memo 20.
Shin, S., Cox, D., 2006. Laboratory observations of inner surf and swash-zone hydrodynamics on a steep slope. Cont. Shelf Res. 26, 573.
Smyth, C., Hay, A.E., 2003. Near-bed turbulence and bottom friction during SandyDuck97. J. Geophys. Res. 108https://doi.org/10.1029/2001JC000952. (C6).
Sou, M., Yeh, H., 2011. Laboratory study of the cross-shore flow structure in the surf and swash zones. J. Geophys. Res. 116, C03002. https://doi.org/10.1029/2010JC006700.
Splinter, K.D., Holman, R.A., Plant, N.G., 2011. A behavior-oriented dynamic model for sandbar migration and 2DH evolution. J. Geophys. Res. 116, C01020. https://doi.org/10.1029/2010JC006382.
Ting, F.C.K., Kirby, J.T., 1994. Observation of undertow and turbulence in a laboratory surf zone. Coast. Eng. 24, 51–80.
Ting, F.C.K., Kirby, J.T., 1995. Dynamics of surf-zone turbulence in a strong plunging breaker. Coast. Eng. 24, 177–204.
Ting, F.C.K., Kirby, J.T., 1996. Dynamics of surf-zone turbulence in a spilling breaker. Coast. Eng. 27, 131–160.
van der A, D.A., van der Zanden, J., O'Donoghue, T., Hurther, D., Cáceres, I., McLelland, S.J., Ribberink, J.S., 2017. Large-scale laboratory study of breaking wave hydrodynamics over a fixed bar. J. Geophys. Res. Oceans 122, 3287–3310.
van der Werf, J.J., Doucette, J.S., O'Donoghue, T., Ribberink, J.S., 2007. Detailed measurements of velocities and suspended sand concentrations over full-scale ripples in regular oscillatory flow. J. Geophys. Res. 112, F02012. https://doi.org/10.1029/2006JF000614.
van der Zanden, J., van der A, D.A., Hurther, D., Cáceres, I., O'Donoghue, T., Ribberink, J.S., 2017. Suspended sediment transport around a large-scale laboratory breaker bar. Coast. Eng. 125, 51–69.
van Rijn, L.C., Ribberink, J.S., van der Werf, J., Walstra, D.J.R., 2013. Coastal sediment dynamics: recent advances and future research needs. J. Hydraul. Res. 51 (5), 475–493. https://doi.org/10.1080/00221686.2013.849297.
Wiberg, P.L., Harris, C.K., 1994. Ripple geometry in wave-dominated environments. J. Geophys. Res. 99, 775–789.
Wright, L.D., Short, A.D., 1984. Morphodynamic variability of surf zones and beaches: a synthesis. Mar. Geol. 56, 93–118.
Yoon, H.-D., Cox, D.T., 2010. Large-scale laboratory observations of wave breaking turbulence over an evolving beach. J. Geophys. Res. 115, C10007. https://doi.org/10.1029/2009JC005748.
Yoon, H.-D., Cox, D.T., 2012. Cross-shore variation of intermittent sediment suspension and turbulence induced by depth-limited wave breaking. Cont. Shelf Res. 47, 93–106.